Electronic Supplementary Material (ESI) for Journal of Materials Chemistry A.

Elucidating the Reaction Pathway of Multi-metal Borides for Highly Efficient Oxygen-Evolving Electrocatalysts

Shijing Zhao [a], Shishuai Xu[b,l], Jinlei Yao[c], Ning Chen[d], Yutong Gong[e], Xipeng Zhang[f], Xianfeng Hao[f], Lijuan Zhang[g], Cuiying Pei[h], Ruifeng Tian[b], Lailei Wu[b], Biao Wan[i], Wenfeng Peng[a], Bo Gao[a], Yanpeng Qi[h], Faming Gao[f], Rajeev Ahuja[j], Yansun Yao[k], Huiyang Gou [a*]

[a] Center for High Pressure Science and Technology Advanced Research, Beijing 100094, China

[b] State Key Laboratory of Metastable Materials Science and Technology, Yanshan University, Qinhuangdao 066004, China

[c] Jiangsu Key Laboratory of Micro and Nano Heat Fluid Flow Technology and Energy Application, School of Mathematics and Physics, Suzhou University of Science and Technology, Suzhou 215009, China

[d] Canadian Light Source Saskatoon, Saskatchewan S7N2V3, Canada

[e] International Center for Materials Discovery, School of Materials Science and Engineering, Northwestern Polytechnical University, Xi'an 710072 Shaanxi, P.R. China

[f] Key Laboratory of Applied Chemistry, College of Environmental and Chemical Engineering, Yanshan University, Qinhuangdao 066004, P.R. China

[g] Shanghai Synchrotron Radiation Facility, Shanghai Advanced Research Institute, Chinese Academy of Sciences, China

[h] School of Physical Science and Technology, ShanghaiTech University, 393 Middle Huaxia Road, Shanghai 201210, China

[i] Key Laboratory of Material Physics of Ministry of Education, School of Physics and Microelectronics, Zhengzhou University, Zhengzhou 450052, China

[j] Department of Physics & Astronomy, Uppsala University, Sweden

[*k*] Department of Physics and Engineering Physics, University of Saskatchewan, Saskatoon, Saskatchewan S7N 5E2, Canada

[l] School of Materials Science and Engineering, Anyang Institute of Technology, Anyang 455000, China

*Correspondence should be addressed to: huiyang.gou@hpstar.ac.cn

Experimental Section

1. Synthesis.

Chemical reagent: cobalt powder (purity >99.9%; diameter ~60 nm; Aladdin), iron powder (purity > 99.9%; diameter ~60 nm; Aladdin), molybdenum powder (purity >99.9%; diameter ~60 nm; Aladdin), boron powder (purity >99.9%; diameter, <20μm; Aladdin), Potassium hydroxide (KOH, 95%; Aladdin), Nafion (Alfa Aesar).

All the materials were used without any further purification in this experiment. The samples were synthesized using a high-temperature and high-pressure (HTHP) technique in a cubic multi-anvil (cubic press) system (CS−1B type, Guilin, China).

Single substances were weighted at a unique ratio and put into an agate mortar, then mixed for more than half hour in a glovebox to guarantee a homogeneous powder. The powder was compacted into cylinder shape (about Φ5mm×4mm) under 10 MPa and then the sample was surrounded by an h-BN capsule. The whole capsule was surrounded by a graphite crucible, which works as a heater.

A cubic press was used to synthesize all the samples at 5GPa. The temperature was raised to 1450/1500℃ at 10℃/s and held for half an hour, then powered down. The samples were placed into an agate mortar and crushed after cleaning. XRD was used to characterize the phase of the samples, ensuring their purity. Finally, more samples were crushed into a fine powder by ball-milling, using a planetary-type high-energy ball mill with a ball to power ratio of 20:1 at 350 rpm for 10h under an Ar atmosphere, in preparation for other characterizations.

2. Morphology and structure characterizations

A spherical aberration correction field emission electron microscope (JEOL JEM 200F) was used to observe the morphologies of the samples and high-resolution TEM images, and electron energy loss spectrum (EELS) elements mapping was also performed. X-ray diffraction (XRD) patterns were obtained using an X-ray diffractometer (PANalytical Empyrean powder X-ray diffractometer) with Cu Kα radiation (λ=1.54Å) at a voltage of 40kV and a current of 40mA. A scanning electron microscope (SEM) was used to detect the sample particle size and the changes of morphology before and after OER. Energy Dispersive Spectroscopy (EDS) was also performed to acquire an elements distribution map. The surface electronic states of various elements were determined by X-ray photoelectron spectroscopy (XPS) using an ESCALAB 250Xi X-ray photoelectron spectrometer with a monocharonmatic X-ray source (Al Kα 1486.6eV). Electrochemical properties were tested

by an electrochemical workstation (CHI 760E, Chenhua, Shanghai). The ex-situ Fe K-edge and Co K-edge Extended X-ray Absorption Fine Structure (EXAFS) data were collected on the Hard X-ray Micro Analysis (HXMA) beamline at the Canadian Light Source. Soft X-ray absorption (XAS) measurements were performed on the BL08U1-A beamline at the Shanghai Synchrotron Radiation facility (SSRF) using the total electron yield (TEY) mode.

3. Electrochemical measurements.

For the oxygen evolution reaction, 5mg samples mixed with 35uL Nafion were dissolved into a 1mL water and ethanol mixture (water：ethanol=1:3), then the solution was dispersed by ultrasonic waves for more than 30 minutes to obtain a stable suspension. A liquid-transferring gun was used to take out the suspension and drop it on carbon cloth to air dry for four hours. The electrochemical properties of the samples were measured by a three-electrode system where a carbon rod works as a counter electrode and the electrolyte was a 1 M KOH solution. The OER properties of different samples were tested by the LSV (linear sweep voltammetry) mode with a scan rate of 5mV/s and electrochemical impedance spectra (EIS) were obtained at 0.6V vs. Hg/HgO electrode in a frequency range from 100k Hz to 0.01 Hz. ECSA (Electrochemical Surface Area) was estimated by measuring the double-layer capacitance formed at the electrode/electrolyte interface carried out in the CV (cyclic voltammetry) mode with a scan rate of 10mV/s, 20mV/s, 40mV/s, 60mV/s, and 80mV/s ranging from 0.2V to 0.3V vs. SCE (saturated calomel electrode). To obtain a precise ECSA value, the samples were deposited on the glassy carbon electrode. Long-term durability was conducted at a potential of 1.54V vs. RHE. The materials were deposited on carbon cloth and measured in a CV model at a rate of 100mV/s from 1.23V vs. RHE to a potential where the current density was 50mA/ cm^2, after reaction for about 30 minutes, the samples were collected as materials after the OER(CV). All potentials of this study are based on a reference reversible hydrogen electrode (RHE):

$E(RHE) = E(Hg/HgO) + 0.098V + 0.0591 \times pH$

$E(RHE) = E(Hg/Hg_2Cl_2) + 0.2415V + 0.0591 \times pH$

$E(RHE) = E(Hg/Hg_2SO_4) + 0.616V + 0.0591 \times pH$

The overpotential (η) was calculated according to the formula: $\eta = E(RHE) - 1.23$ V.

Tafel slopes were obtained from the linear part of Tafel curve obtained with the reference formula:

$\eta = b*\log(j)+a$

For the hydrogen evolution reaction, the sample preparation method is the same. The electrochemical properties of the samples were measured by a three-electrode system where a carbon rod works as a counter electrode and the electrolyte was a 0.5 M H_2SO_4 solution. The HER properties of different samples were tested by the LSV (linear sweep voltammetry) mode with a scan rate of 5mV/s. ECSA(Electrochemical Surface Area) was estimated by measuring the double-layer capacitance formed at the electrode/electrolyte interface carried out in the CV (cyclic voltammetry) mode with a scan rate of 10mV/s, 20mV/s, 30mV/s, 40mV/s, and 50mV/s ranging from -0.5V to -0.6V vs. Hg/Hg_2SO_4 electrode. The materials were deposited on carbon cloth and measured in a CV model at a rate of 100mV/s from -0.6V to -1.3V vs. Hg/Hg_2SO_4 electrode. after reaction for about 30 minutes, the samples were collected as materials after the HER.

4. Calculations.

The Density Functional Theory (DFT) calculations were achieved with the plane wave basis set as implemented in the Vienna *ab initio* simulation package[1,2]. The generalized gradient approximation (GGA) exchange correlation functional was adopted according to the Perdew-Burke-Ernzerhof scheme[3] to investigate the electronic properties. The convergence criteria for the self-consistent field and geometry optimization were set to 10^{-5} eV and 10^{-2} eV/Å, respectively. The energy cutoff for the plane wave expansion was 500 eV, which guarantees excellent convergence. In addition, the *k*-point meshes over the total Brillouin zone were sampled by 10×10×3 grids constructed according to the Monkhorst-Pack scheme[4,5]. The density of states was calculated using the tetrahedron method. Fe_2MoB_4 crystallized in an orthorhombic phase with *Immm* space group with Z = 2. The crystal structure is constructed of mirror-symmetric layers consisting of two staggered, inverted sheets of FeB_7 polyhedra along the *c* axis, which are joined together by the Mo atoms located in the mirror plane. To identify the magnetic ground state, we tentatively evaluated the total energies of the nonmagnetic (NM), ferromagnetic (FM) and two antiferromagnetic (AFM) configurations based on the aforementioned settings. In the AFM-I pattern, the magnetic coupling within the two-sheet staggered FeB_7 layers is ferromagnetic, while the coupling between the stacking layers is antiferromagentic along the *c* direction. On the other hand, spins on the Fe atoms are antiparallel to each other within the two-sheet inverted layers within the AFM-II one.

We enumerated all the potential configurations of the Co-doped $Fe_{2-x}Co_xMoB_4$ (x = 0, 0.5, 1, 1.5 and 2) systems within the conventional unit cell. According to our symmetry analysis, there is only

one pattern for all the doping cases except for x=1. Clearly, two configurations should be considered in this special case, in which the two Co atoms can be entirely distributed within one two-sheet layers, or evenly located at the mirror-symmetric lay.

Table S1. Mulliken overlap population of the different bonds in *MM*MoB_4 (*M*=Fe, Co).

Bond	MOP	MOP	Bond	MOP	Bond	MOP	MOP
Fe_2MoB_4							
B-B	1.19	0.83	B-Mo	0.05	B-Fe	0.18	0.31
Fe-Fe	0.14	0.21					
$CoFeMoB_4$							
B-B	1.19	0.83	B-Mo	0.05			
B-Fe	0.19	0.31					
B- Co	0.16	0.17	0.3				
Fe-Co	0.13						
Fe-Fe	0.15						
Co_2MoB_4							
B- B	1.19	0.82	B-Mo	0.05	B-Co	0.16	0.33
Co-Co	0.14						

Table S2. Comparison of the catalytic properties (OER) of different boride catalysts recently reported in KOH solution.

Materials and morphology	Synthesize method	Mass loading (mg/cm^2)	η10(mV)	electrolyte	Substrate	Tafel slope ($mVdec^{-1}$)	Ref.
Ni-Co-B	$NaBH_4$	4	300	1M KOH	NF	113	[6]
Ni-Co-B/rGO nanosheets	$NaBH_4$	0.2	280	1M KOH	GCE	56	[7]
Fe3Co7-B/CNT	$NaBH_4$	0.3	265	1M KOH	GCE	30	[8]
Co-B/NF nanosheets	$NaBH_4$	8	265($_{\eta 20}$)	1M KOH	NF	55.6	[9]
NiB/Ni	Boronizing	-	300	1M KOH	Ni plate	43	[10]
Co2B nanoparticles	$NaBH_4$	0.21	360	1M KOH	GCE	45	[11]
FeCo2.3NiB nanoparticle	$NaBH_4$	0.3	274	1M KOH	GCE	38	[12]
Co-Mo-B nanoparticles	$NaBH_4$	2.1	320	1M NaOH	GCE	155	[13]
NixB nanoparticles	$NaBH_4$	0.21	380/280	1M KOH	GCE/NF	-	[14]
CoNiB nanoparticles	$NaBH_4$	1.4	313	-	NF	131	[15]
Ni-B_i@N_3B nanoparticles	$NaBH_4$	0.3	302	1M KOH	GCE	52	[16]
$NiB_{0.45}/NiO_x$ nanoparticles	$NaBH_4$	-	296	1M KOH	Cu	58	[17]
Co-B@CoO/Ti nanoarray	$NaBH_4$	5.87	190	1M KOH	Ti	78	[18]
FeB_2 nanoparticles	$LiBH_4$	0.2	296	1M KOH	GCE	52.4	[19]
CoB/NCNT	$NaBH_4$	0.21	370	0.1M KOH	GCE	-	[20]
Co2-Fe-B nanoparticles	$NaBH_4$	1.2	298	1M KOH	Cu	62.6	[21]
Co-B/C	$NaBH_4$	0.16	320	1M KOH	GCE	75	[22]
Ni_3B-rGO nanocomposite	$NaBH_4$	0.2	290	1M KOH	CP	88.4	[23]
NiFeB nanoparticles	$NaBH_4$	0.2	251	1M KOH	GCE	43	[24]
FeNiB nanosheets	$NaBH_4$	1	237	1M KOH	NF	38	[25]
CoB nanosheets	$NaBH_4$	12	315	1M KOH	NF	80	[26]
NiCoFeB nanochains	$NaBH_4$	0.375	284	1M KOH	GCE	46	[27]
CoB_x@h-BN nanoparticles	KBH_4	0.16	290	1M KOH	GCE	98.6	[28]
CoB	C2H10BN	2.4	140	1M KOH	NF	98	[29]
$(Co_{0.7}Fe_{0.3})_2B$ nanorods	$NaBH_4$	0.375	330	1M KOH	GCE	40	[30]
NiB/$Ni(OH)_2$/Ni	$NaBH_4$	1.03	300($_{\eta 100}$)	1M KOH	NF	49	[31]
FeNi3-B/GO	$NaBH_4$	0.3	230($_{\eta 15}$)	1M KOH	GCE	50	[32]
Ni_xB/f-MWCNT	$NaBH_4$	0.2	370	1M KOH	GCE	46.3	[33]
NiBO@Ni_XB nanoparticles	$NaBH_4$	1.6	219	1M KOH	NF	80.9	[34]

TiB_2/FTO	$NaBH_4$	2	560	1M $HClO_4$	GCE	-	[35]
AlFe2B2	Arc-melt	1	240	1M KOH	NF	42	[36]
Boronized NiFe	Boronizing	-	309	1M KOH	NiFe sheet	40	[37]
Fe-B-O@Fe_xB	$NaBH_4$	2.8	260	1M KOH	NF	57.9	[38]
Co-B@Co-Bi	$NaBH_4$	0.3	291	1M KOH	GCE	120.73	[39]
VCoNiB	$NaBH_4$	0.285	280($_{\eta 30}$)	1M KOH	NF	58	[40]
$CoFeMoB_4$		4	251	1M KOH	CC	27.2	This work

Table S3. Fitted peaks' position and valences of different elements before and after OER from XPS results.

Phase	As-prepared		After CV	
	Species	Peak position(eV)	Species	Peak position(eV)
$CoFeMoB_4$	Co^0	778.53; 793.58	Co^0	778.70; 793.68
	$Co^{2+}(2p_{3/2})$	781.58; 786.52	$Co^{2+}(2p_{3/2})$	782.00; 786.50
	$Co^{2+}(2p_{1/2})$	797.57; 803.65	$Co^{2+}(2p_{1/2})$	797.80; 803.80
	Fe^0	707.18; 720.23		
	$Fe^{2+}(2p_{3/2})$	710.15; 714.06	$Fe^{3+}(2p_{3/2})$	711.23; 715.30
	$Fe^{2+}(2p_{1/2})$	723.97; 729.04	$Fe^{3+}(2p_{1/2})$	724.44; 730.32
	Mo^0	228.16; 231.34		
	Mo^{3+}	228.80	Mo^{3+}	
	Mo^{6+}	232.73; 235.66	Mo^{6+}	232.44; 235.50
	B^0	188.46		
	B^{3+}	192.59	B^{3+}	192.18
	O	531.90	O	532.27
Co_2MoB_4	Co^0	778.37; 793.37		
	$Co^{2+}(2p_{3/2})$	781.29; 785.93	$Co^{3+}(2p_{3/2})$	780.97; 785.15
	$Co^{2+}(2p_{1/2})$	797.49; 803.28	$Co^{3+}(2p_{1/2})$	796.78; 802.80
	Mo^0	228.11; 231.19	Mo^0	228.29
	Mo^{3+}	229.22		
	Mo^{6+}	232.60; 235.57	Mo^{6+}	232.34; 235.48
	B^0	188.34	B^0	188.55
	B^{3+}	192.54	B^{3+}	192.12
	O	531.78	O	531.34
			O	535.47
Fe_2MoB_4	Fe^0	706.92; 719.96		
	$Fe^{2+}(2p_{3/2})$	709.99; 714.49	$Fe^{3+}(2p_{3/2})$	711.06; 715.02
	$Fe^{2+}(2p_{1/2})$	723.46; 728.28	$Fe^{3+}(2p_{1/2})$	724.48; 729.30
	Mo^0	227.98; 231.10		
	Mo^{3+}	228.97		
	Mo^{6+}	232.42; 235.52	Mo^{6+}	232.45; 235.47
	B^0	188.21	B^0	188.28
	B^{3+}	192.37	B^{3+}	192.18
	O	530.64		
	O	531.86	O	532.48

Table S4. Partial parameters related to oxides and (oxy)hydroxides in the fitting results of Co, Fe, and Mo K-edge EXAFS of $CoFeMoB_4$ after OER with different models. χ^2 is a value used to evaluate the fitting results, where smaller is better [41].

Co_2MoB_4+$Co(OH)_2$				Co_2MoB_4+CoOOH				Co_2MoB_4+CoO			
Path	R(Å)	CN	χ^2	Path	R(Å)	CN	χ^2	Path	R(Å)	CN	χ^2
Co-O	2.06	4.3	931	Co-O	2.07	4.4	1257	Co-O	2.04	1.8	1336
Co-Co	3.15	4.6		Co-Co	2.86	5.8		Co-Co	3.10	10.5	
				Co-O	3.65	6.3		Co-O	3.77	3.2	
Fe_2MoB_4+Fe_2O_3				Fe_2MoB_4+FeOOH				Co_2MoB_4+MoO_3			
Path	R(Å)	CN	χ^2	Path	R(Å)	CN	χ^2	Path	R(Å)	CN	χ^2
Fe-O	1.38	0.9	34846	Fe-O	2.01	2.2	13269	Mo-O	1.73	1.8	1214
Fe-O	1.57	0.9		Fe-Fe	3.03	5.8		Mo-O	2.17	1.2	
Fe-O	2.38	1.3		Fe-O	3.83	7.7		Mo-O	2.49	0.6	
Fe-Fe	3.21	2.6						Mo-O	2.48	1.0	
								Mo-Mo	3.04	1.6	
Co_2MoB_4+$K_2Mo_2O_7 \cdot H_2O$											
Path	R(Å)	CN	χ^2								
Mo-O	1.71	0.8	775								
Mo-O	1.76	1.0									
Mo-O	1.78	0.8									
Mo-O	2.36	2.9									
Mo-Mo	3.23	1.5									
Mo-O	2.90	0.6									

Table S5. Fitting result parameters of Co K-edge EXAFS of $CoFeMoB_4$ after OER with a structural model of Co_2MoB_4 and Co $(OH)_2$ (paths in blue).

	$CoFeMoB_4$+$Co(OH)_2$					
Path	R(Å)	CN	χ^2	E_0 shift	σ^2	
1.Co-O	2.06	4.3	931	-4.85	0.0065	+- 0.000047
2.Co-B	2.00	3.9			0.0100	+- 0.000183
3.Co-B	2.45	1.2			0.0055	+- 0.000289
4.Co-Mo	2.74	1.4			0.0056	+- 0.000052
5.Co-Co/Fe	2.74	3.9			0.0073	+- 0.000152
6.Co-Co/Fe	3.00	4.4			0.0071	+- 0.000051
7.Co-Co	3.15	4.6			0.0091	+- 0.000132
8.Co-B	3.40	5.6			0.0050	+- 0.000341
9.Co-B	3.78	5.6			0.0050	+- 0.000179

Table S6. Fitting result parameters of Co K-edge EXAFS of $CoFeMoB_4$ after OER with a structural model of Co_2MoB_4 and CoOOH (paths in blue).

	$CoFeMoB_4$+CoOOH					
Path	R(Å)	CN	χ^2	E_0 shift	σ^2	
1.Co-O	2.07	4.4	1257	-0.0873	0.0085	+- 0.000017
2.Co-B	2.56	5.2			0.0076	+- 0.000394
3.Co-B	2.49	0.8			0.005	+- 0.000546
4.Co-Mo	2.82	1.6			0.0079	+- 0.000227
5.Co-Co/Fe	2.68	4.0			0.0073	+- 0.000152
6.Co-Co	2.86	5.8			0.01	+- 0.000086
7.Co-Co/Fe	3.1	4.0			0.0089	+- 0.000172
8.Co-B	3.32	0.9			0.01	+- 0.005535
9.Co-O	3.65	6.3			0.0076	+- 0.000080
10.Co-B	4.04	13.4			0.01	+- 0.000077

Table S7. Fitting result parameters of Co K-edge EXAFS of $CoFeMoB_4$ after OER with a structural model of Co_2MoB_4 and CoO (paths in blue).

	$CoFeMoB_4$+CoO					
Path	R(Å)	CN	χ^2	E_0 shift	σ^2	
1.Co-O	2.04	1.8	1336	-1.072	0.005	+- 0.000034
2.Co-B	2.22	4.6			0.01	+- 0.000067
3.Co-Mo	2.8	1.4			0.005	+- 0.000061
4.Co-Co/Fe	2.77	4.3			0.0094	+- 0.000077
5.Co-Co/Fe	2.94	4.1			0.0054	+- 0.000105
6.Co-Co	3.1	10.5			0.0093	+- 0.000060
7.Co-B	3.36	14.3			0.005	+- 0.000080
8.Co-O	3.77	3.2			0.0061	+- 0.000117
9.Co-B	3.73	6.0			0.0055	+- 0.000137

Table S8. Fitting result parameters of Co K-edge EXAFS of $CoFeMoB_4$ after OER with a structural model of Co_2MoB_4.

	$CoFeMoB_4$ after OER					
Path	R(Å)	CN	χ^2	E_0 shift	σ^2	
1.Co-B	2.15	7.4	2498	-4.494	0.0058	+- 0.000035
2.Co-B	2.33	1.7			0.005	+- 0.000233
3.Co-Mo	2.78	2.2			0.0053	+- 0.000036
4.Co-Co/Fe	2.77	3.0			0.0097	+- 0.000055
5.Co-Co/Fe	3.06	3.9			0.0095	+- 0.000016
6.Co-B	3.24	4.2			0.01	+- 0.000173
7.Co-B	3.75	9.3			0.007	+- 0.000056
8.Co-B	4	10.1			0.0051	+- 0.000037

Table S9. Fitting result parameters of Co K-edge EXAFS of $CoFeMoB_4$ before OER with a structural model of Co_2MoB_4.

$CoFeMoB_4$ as-prepared						
Path	R(Å)	CN	χ^2	E_0 shift	σ^2	
1.Co-B	2.14	5.2	21921	2.887	0.0064	+- 0.000024
2.Co-B	2.38	3.0			0.0089	+- 0.000104
3.Co-Mo	2.79	1.7			0.005	+- 0.000017
4.Co-Co/Fe	2.73	4.3			0.01	+- 0.000014
5.Co-Co/Fe	3.06	3.9			0.01	+- 0.000025
6.Co-B	3.34	3.8			0.0055	+- 0.000113
7.Co-B	4.05	11.9			0.005	+- 0.000022
8.Co-B	3.77	11.6			0.0098	+- 0.000062

Table S10. Fitting result parameters of Fe K-edge EXAFS of $CoFeMoB_4$ after OER with a structural model of Fe_2MoB_4 and FeOOH (paths in blue).

			$CoFeMoB_4$+FeOOH			
Path	R(Å)	CN	χ^2	E_0 shift	σ^2	
1.Fe-O	2.01	2.2	13269	-3.1559	0.0051	+- 0.000035
2.Fe-B	2.12	2.9		+- 0.0148	0.005	+- 0.000054
3.Fe-Mo	2.78	1.3			0.0055	+- 0.000022
4.Fe-Fe/Co	2.75	4.0			0.0091	+- 0.000041
5.Fe-Fe/Co	2.91	1.6			0.0097	+- 0.000219
6.Fe-Fe	3.03	5.8			0.0098	+- 0.000020
7.Fe-Fe/Co	3.21	2.0			0.0086	+- 0.000098
8.Fe-B	3.25	2.4			0.01	+- 0.001041
9.Fe-O	3.83	7.7			0.01	+- 0.000061
10.Fe-B	3.71	6.6			0.005	+- 0.000069

Table S11. Fitting result parameters of Fe K-edge EXAFS of $CoFeMoB_4$ after OER with a structural model of Fe_2MoB_4 and Fe_2O_3 (paths in blue).

	$CoFeMoB_4$+Fe_2O_3					
Path	R(Å)	CN	χ^2	E_0 shift	σ^2	
1.Fe-O	1.38	0.9	34846	-6.16	0.01	+- 0.000091
2.Fe-O	1.57	0.9			0.0068	+- 0.000067
3.Fe-B	2.11	6.7			0.005	+- 0.000027
4.Fe-O	2.38	1.3			0.0093	+- 0.000258
5.Fe-Mo	2.8	2.3			0.0054	+- 0.000017
6.Fe-Fe/Co	2.74	3.2			0.01	+- 0.000035
7.Fe-Fe	3.21	2.6			0.0071	+- 0.000123
8.Fe-O	2.81	3.9			0.0092	+- 0.000129
9.Fe-Fe/Co	3.13	2.7			0.01	+- 0.000022
10.Fe-Fe/Co	3.33	7.3			0.01	+- 0.000085

Table S12. Fitting result parameters of Fe K-edge EXAFS of $CoFeMoB_4$ after OER with a structural model of Fe_2MoB_4.

			$CoFeMoB_4$ after OER			
Path	R(Å)	CN	χ^2	E_0 shift	σ^2	
1.Fe-B	2.11	6.2	23664	-5.6356	0.005	+- 0.000229
2.Fe-B	2.12	1.0			0.005	+- 0.001388
3.Fe-Mo	2.79	2.0			0.005	+- 0.000026
4.Fe-Fe/Co	2.77	3.9			0.01	+- 0.000026
5.Fe-Fe/Co	2.99	2			0.005	+- 0.000031
6.Fe-Fe/Co	3.13	4.2			0.005	+- 0.000020
7.Fe-B	3.29	1.9			0.01	+- 0.000402
8.Fe-B	3.73	4.2			0.005	+- 0.000086
9.Fe-B	4.01	9.2			0.0069	+- 0.000035

Table S13. Fitting result parameters of Fe K-edge EXAFS of $CoFeMoB_4$ before OER with a structural model of Fe_2MoB_4.

$CoFeMoB_4$ as-prepared						
Path	R(Å)	CN	χ^2	E_0 shift	σ^2	
1.Fe-B	2.15	5.9	51547	1.055	0.0068	+- 0.000020
2.Fe-B	2.37	1.0			0.0066	+- 0.000224
3.Fe-Mo	2.8	1.9			0.0051	+- 0.000022
4.Fe-Fe/Co	2.75	3.9			0.01	+- 0.000014
5.Fe-Fe/Co	3	1.9			0.0087	+- 0.000076
6.Fe-Fe/Co	3.11	1.9			0.0095	+- 0.000078
7.Fe-B	3.21	2.1			0.005	+- 0.000401
8.Fe-B	3.78	7.5			0.005	+- 0.000086
9.Fe-B	4.04	13.2			0.0051	+- 0.000016

Table S14. Fitting result parameters of Mo K-edge EXAFS of $CoFeMoB_4$ after OER with a structural model of Co_2MoB_4.

	$CoFeMoB_4$ after OER					
Path	R(Å)	CN	χ^2	E_0 shift	σ^2	
1.Mo-B	2.27	11.5	5278	-6	0.0077	+- 0.000148
2.Mo-B	2.48	20.1			0.01	+- 0.000147
3.Mo-Co/Fe	2.74	3.8			0.0099	+- 0.000133
4.Mo-Mo	3.06	2.9			0.0091	+- 0.000137
5.Mo-B	3.51	6.0			0.0061	+- 0.000173
6.Mo-Co/Fe	4.16	4.6			0.01	+- 0.000168
7.Mo-Co/Fe	4.3	3.3			0.005	+- 0.000283
8.Mo-Mo	4.32	4.6			0.0068	+- 0.000225

Table S15. Fitting result parameters of Mo K-edge EXAFS of $CoFeMoB_4$ before OER with a structural model of Co_2MoB_4.

$CoFeMoB_4$ as-prepared						
Path	R(Å)	CN	χ^2	E_0 shift	σ^2	
1.Mo-B	2.24	4	42725	-3.1064	0.01	+- 0.000052
2.Mo-B	2.38	7.0			0.005	+- 0.000013
3.Mo-Co/Fe	2.79	3.3			0.0089	+- 0.000012
4.Mo-Mo	3.01	3.9			0.01	+- 0.000014
5.Mo-B	3.73	8			0.01	+- 0.000081
6.Mo-Co/Fe	4.2	4.3			0.0051	+- 0.000045
7.Mo-Co/Fe	4.4	2.6			0.005	+- 0.000083
8.Mo-Mo	4.34	2.5			0.005	+- 0.000043

Table S16. Fitting result parameters of Mo K-edge EXAFS of $CoFeMoB_4$ after OER with structural model of Co_2MoB_4 and $K_2Mo_2O_7 \cdot H_2O$ (paths in blue).

$CoFeMoB_4$ + $K_2Mo_2O_7 \cdot H_2O$						
Path	R(Å)	CN	χ^2	E0 shift	σ^2	
1.Mo-O	1.71	0.8	775	-2.7837	0.01	+- 0.000611
2.Mo-O	1.76	1.0			0.005	+- 0.000698
3.Mo-O	1.78	0.8			0.005	+- 0.000775
4.Mo-B	2.18	2.8			0.0051	+- 0.000292
5.Mo-O	2.36	2.9			0.0067	+- 0.000216
6.Mo-B	2.33	7.4			0.0067	+- 0.000160
7.Mo-Co	2.79	3.6			0.0097	+- 0.000010
8.Mo-Mo	3.05	3.9			0.01	+- 0.000172
9.Mo-Mo	3.23	1.5			0.0057	+- 0.000210
10.Mo-O	2.9	0.6			0.0075	+- 0.002429
11.Mo-B	3.54	12.6			0.01	+- 0.000154
12.Mo-K	3.69	1.9			0.005	+- 0.001750

Table S17. Fitting models.

	Co_2MoB_4（Co）			Fe_2MoB_4（Fe）			Co_2MoB_4（Mo）		
	Path	R(Å)	CN	Path	R(Å)	CN	Path	R(Å)	CN
1	Co-B	2.19	2	Fe-B	2.22	2	Mo-B	2.2	4
2	Co-B	2.26	4	Fe-B	2.27	4	Mo-B	2.27	8
3	Co-B	2.45	1	Fe-B	2.48	1	Mo-Co	2.72	4
4	Co-Mo	2.72	2	Fe-Mo	2.73	2	Mo-Mo	3.05	4
5	Co-Co	2.78	4	Fe-Fe	2.8	4	Mo-B	3.73	8
6	Co-Co	3.02	2	Fe-Fe	2.98	2	Mo-Co	4.11	8
7	Co-Co	3.08	2	Fe-Fe	3.13	2	Mo-Co	4.31	4
8	Co-B	3.34	2	Fe-B	3.38	2	Mo-Mo	4.31	4
9	Co-B	3.65	2	Fe-B	3.67	2			
10	Co-B	3.73	4	Fe-B	3.72	4			
11	Co-B	3.89	2	Fe-B	3.88	2			
	CoOOH			Co $(O H)_2$			CoO		
	Path	R(Å)	CN	Path	R(Å)	CN	Path	R(Å)	CN
1	Co-O	1.9	6	Co-O	2.1	6	Co-O	2.14	6
2	Co-H	2.75	6	Co-Co	3.17	6	Co-Co	3.03	12
3	Co-Co	2.86	6	Co-O	3.8	6	Co-O	3.71	8
4	Co-O	3.43	6	Co-O	4.06	6	Co-Co	4.28	6
5	Co-O	3.83	6	Co-Co	4.64	2	Co-O	4.78	24
6	Co-H	3.94	6				Co-Co	5.24	24
	Fe_2O_3			FeOOH			Mo O_3		
	Path	R(Å)	CN	Path	R(Å)	CN	Path	R(Å)	CN
1	Fe-O	1.31	1	Fe-O	2	6	Mo-O	1.67	1
2	Fe-O	2.11	1	Fe-H	2.87	4	Mo-O	1.73	1
3	Fe-O	2.53	2	Fe-Fe	3.05	6	Mo-O	1.95	2
4	Fe-O	2.98	2	Fe-O	3.65	6	Mo-O	2.25	1
5	Fe-Fe	3.29	8	Fe-Fe	3.87	2	Mo-O	2.33	1
6	Fe-O	3.64	3	Fe-H	3.97	4	Mo-Mo	3.44	2
7	Fe-O	3.76	1	Fe-O	4.01	4	Mo-O	3.55	4
8	Fe-Fe	4.02	1				Mo-Mo	3.7	2
	$K_2Mo_2O_7 \cdot H_2O$								
	Path	R(Å)	CN						
1	Mo-O	1.74	2						
2	Mo-O	1.82	1						
3	Mo-O	2.05	1						
4	Mo-O	2.24	2						
5	Mo-Mo	3.24	2						
6	Mo-O	3.59	1						
7	Mo-Mo	3.83	1						
8	Mo-K	3.84	2						

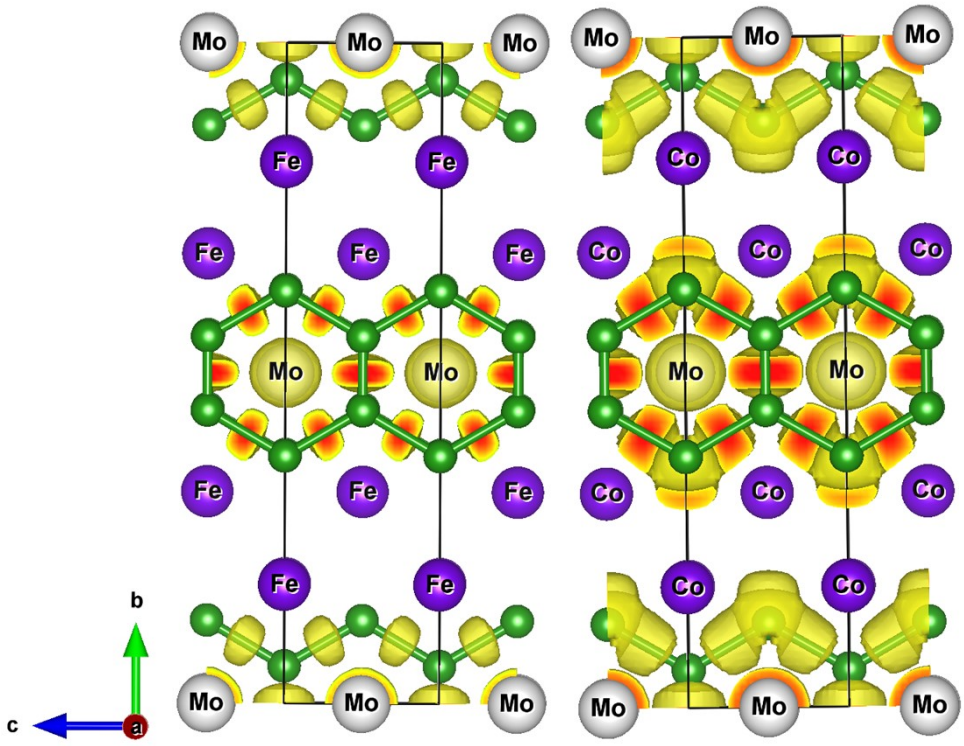

Figure S1. ELF (Electron Localization Function) of Fe_2MoB_4 and Co_2MoB_4.

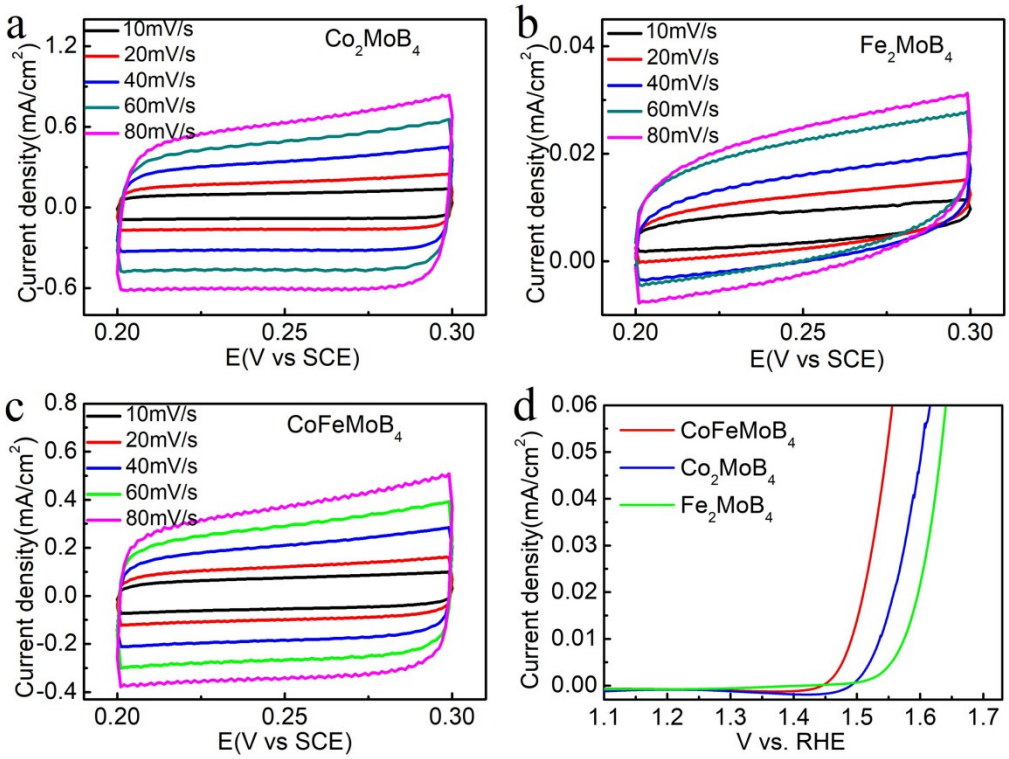

Figure S2. CV curves at different scan rates of (a) Co_2MoB_4, (b) Fe_2MoB_4, and (c) $CoFeMoB_4$; (d) ECSA normalized LSC curves[42].

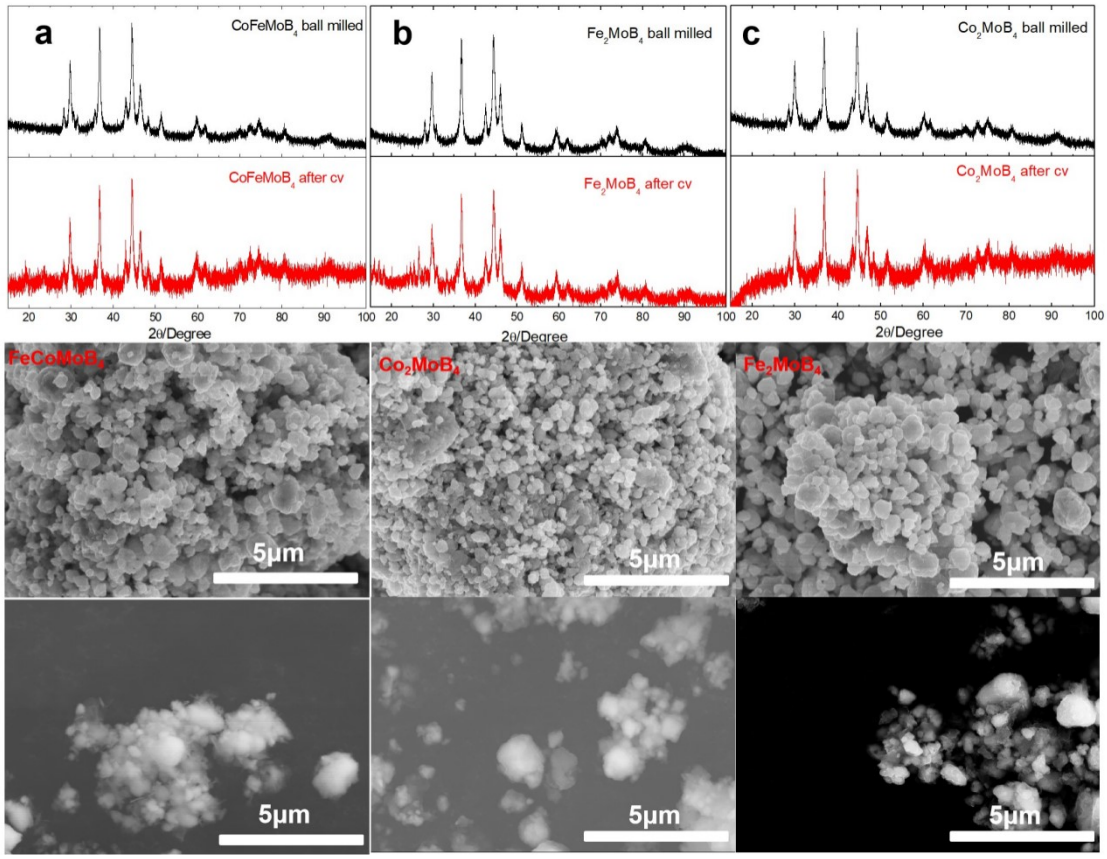

Figure S3. XRD patterns of (a) $CoFeMoB_4$, (b) Co_2MoB_4 and (c) Fe_2MoB_4 before (black line) and after CVs tested (red line). Corresponding SEM images of samples before and after OER are below the XRD patterns.

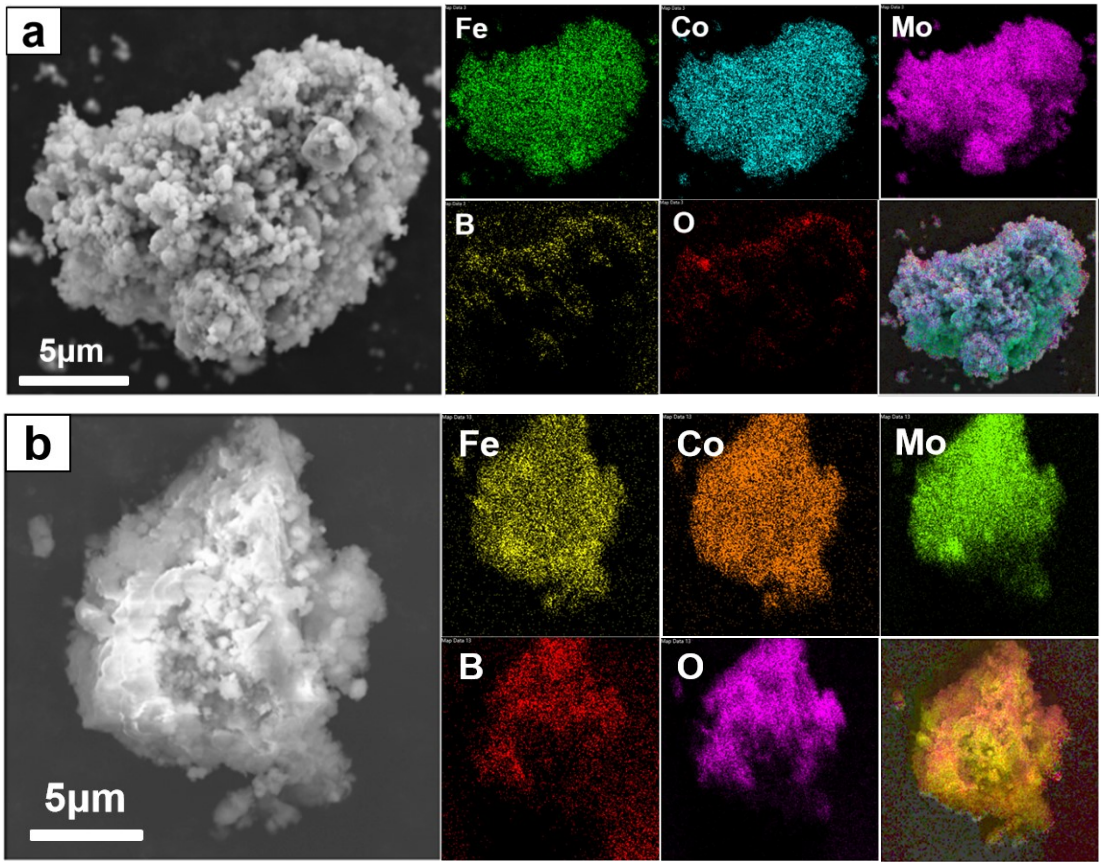

Figure S4. SEM images and corresponding element mapping for $CoFeMoB_4$. (a) As-prepared sample. (b) Sample after OER.

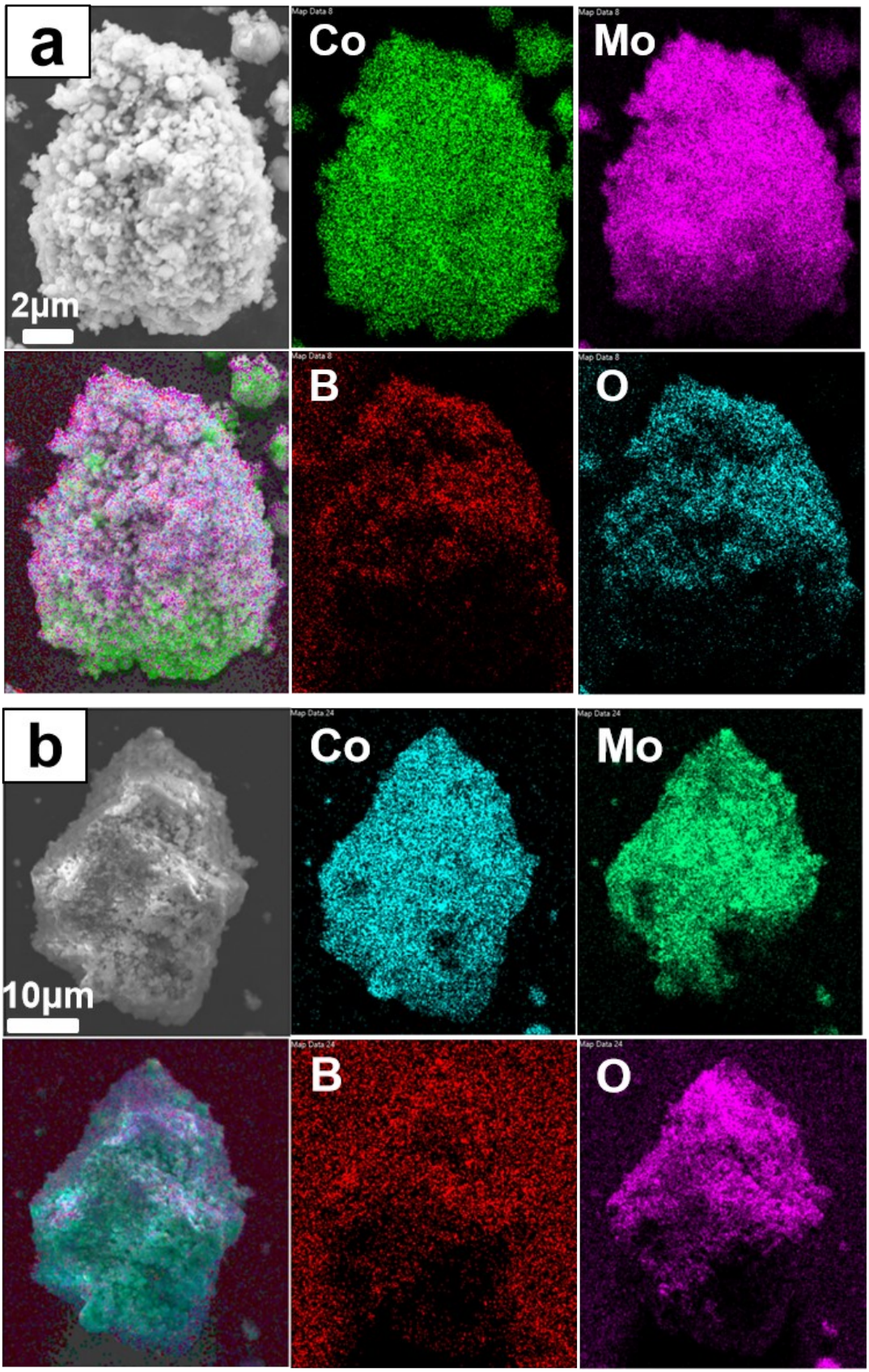

Figure S5. SEM images and corresponding element mapping for Co_2MoB_4. (a) As-prepared sample. (b) Sample after OER.

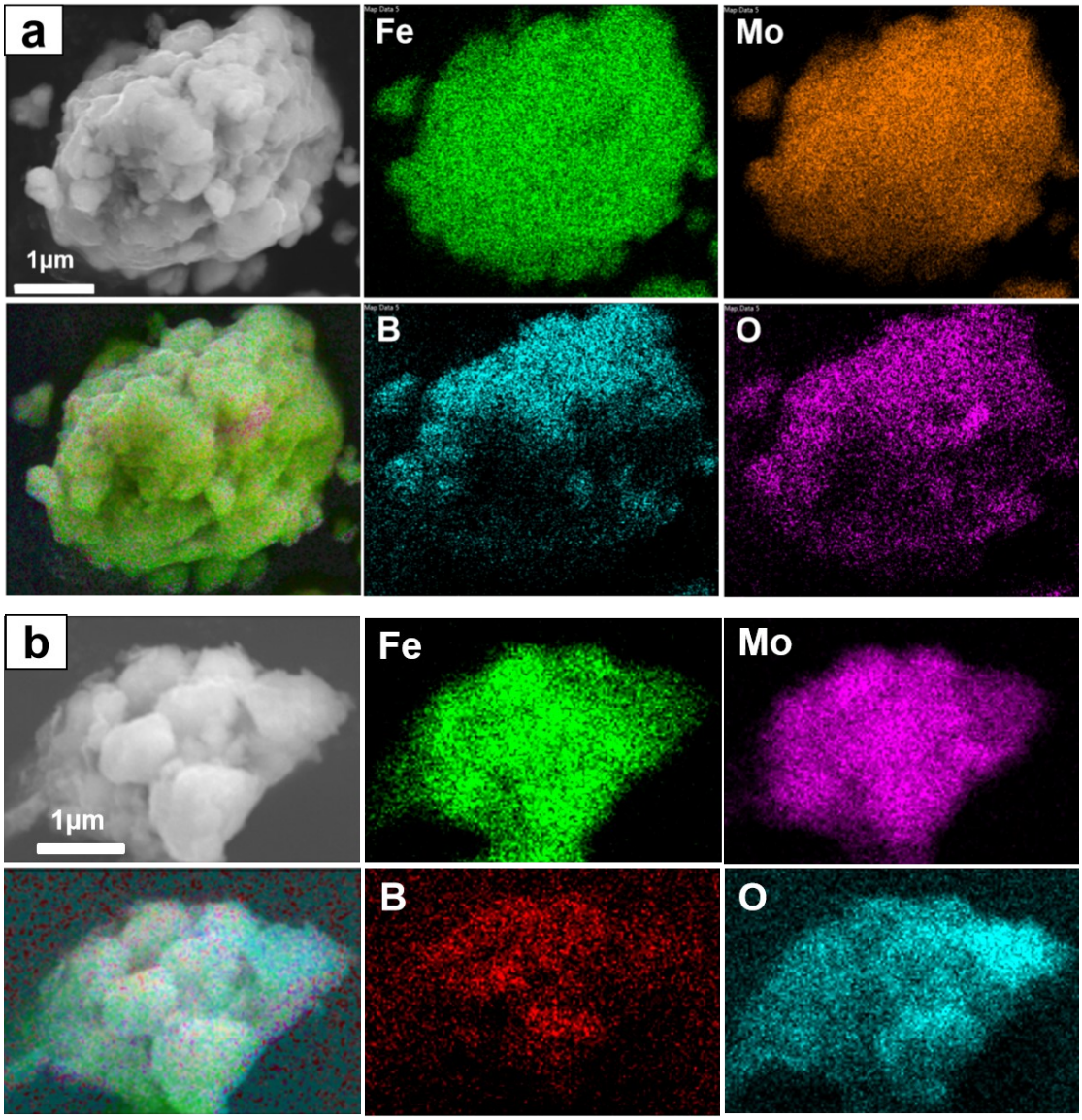

Figure S6. SEM images and corresponding element mapping for Fe_2MoB_4. (a) As-prepared sample. (b) Sample after OER.

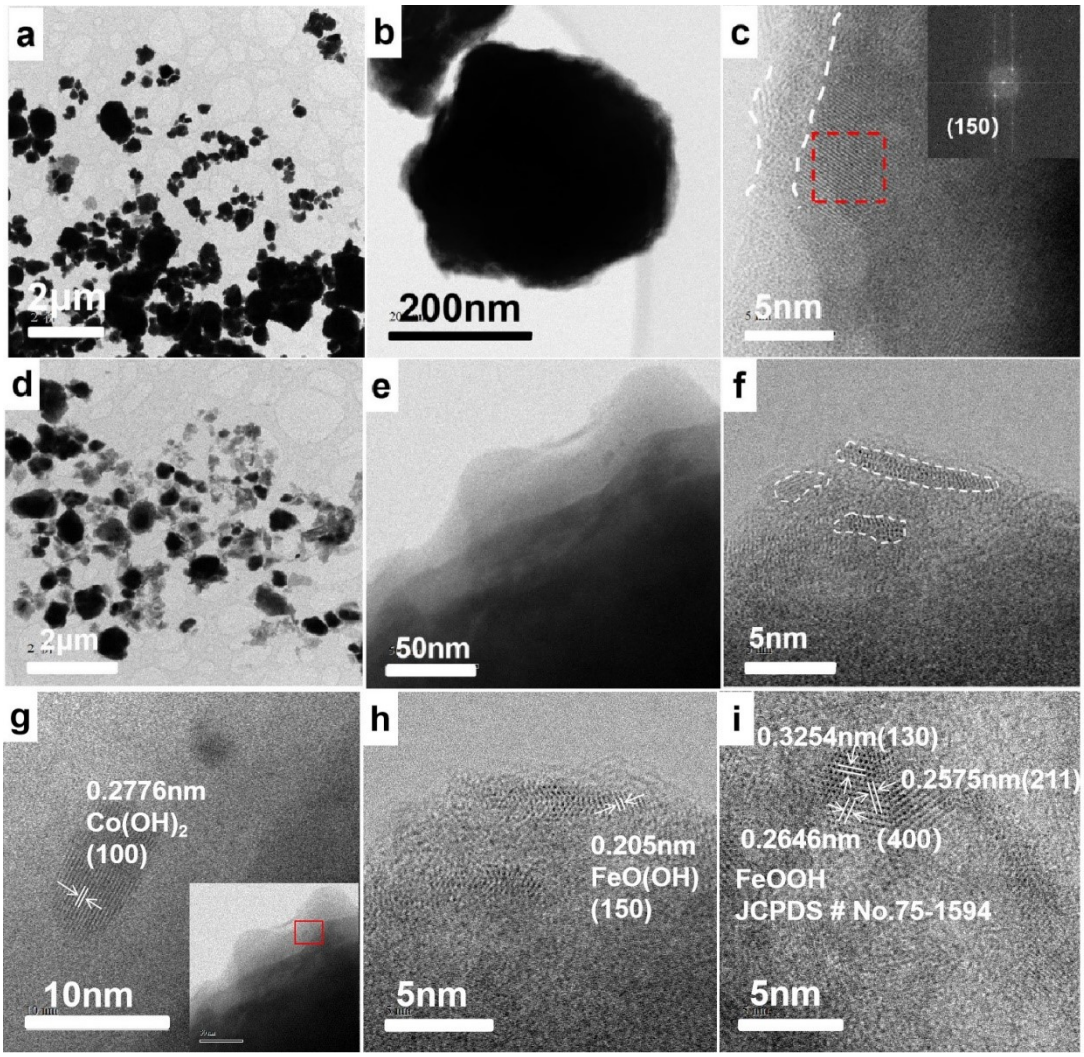

Figure S7. (a), (d) TEM morphology image of $FeCoMoB_4$ before and after OER. (b)TEM image of a single $FeCoMoB_4$ particle. (c) HRTEM image of the particle edge. Inset shows Fourier transform image for $FeCoMoB_4$ before OER. (e) TEM morphology image of single $FeCoMoB_4$ particle edge after OER. (f) HRTEM for edge area shows the microcrystal and amorphous phase coexisting. (g) High-angle annular dark field TEM of $CoFeMoB_4$. (h) and (i) HRTEM of FeOOH on surface layer of $CoFeMoB_4$.

Figure S8. (a) High-angle annular dark field TEM of $CoFeMoB_4$. (b) and (c) are enlarged images of A and B in (a). (d) Enlarged image of B in (a). (e) Enlarged image of D from (d). (f) EELS elements mapping of $CoFeMoB_4$ after OER.

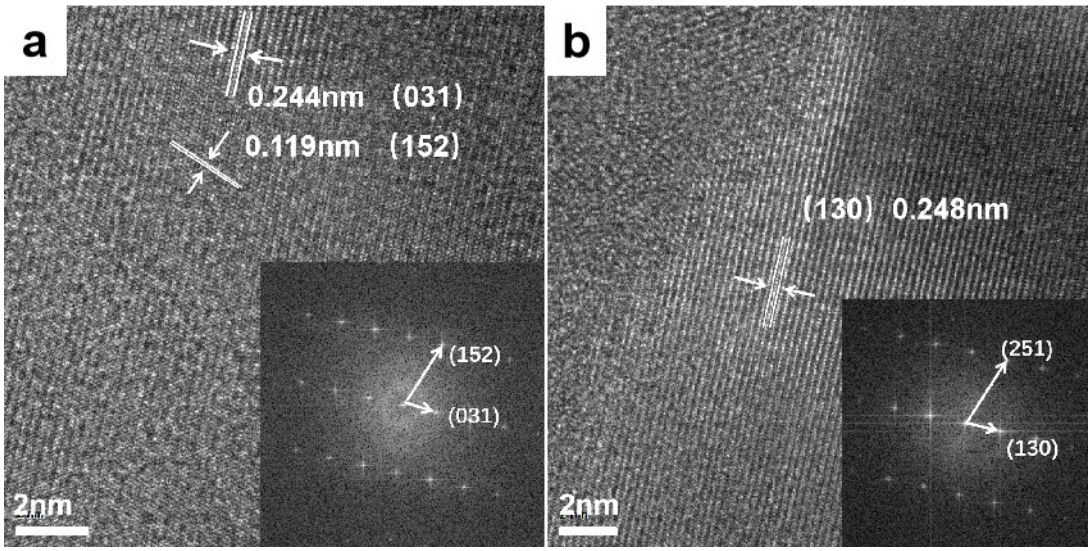

Figure S9. High-angle annular dark field TEM images of as-prepared Co_2MoB_4 different plane spacing and corresponding Fourier transform images. (a) and (b) are different area.

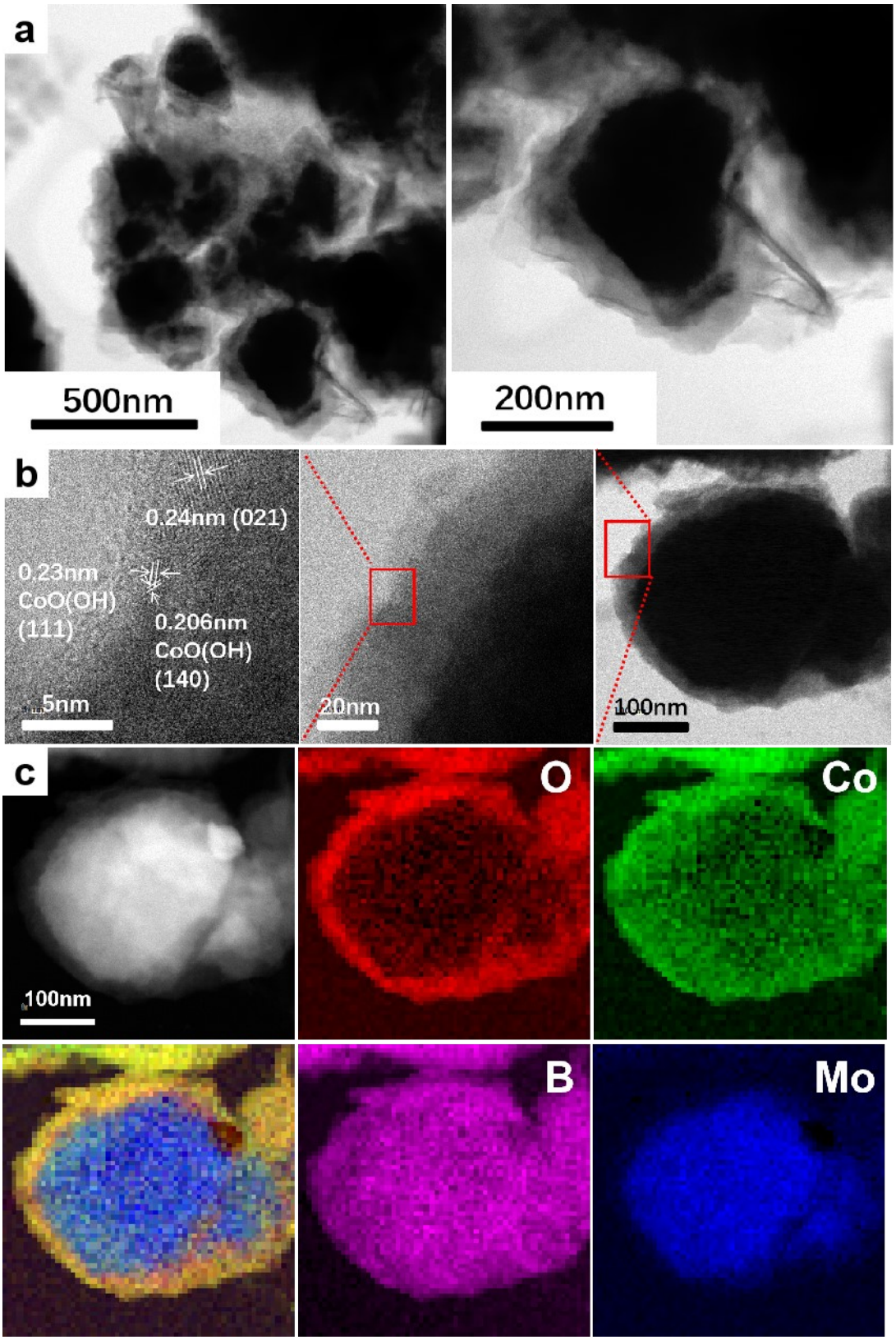

Figure S10. (a) The TEM morphology images of Co_2MoB_4 after OER. (b) High-angle annular dark field TEM images of Co_2MoB_4 after OER. (c) EELS mapping of Co_2MoB_4 after OER.

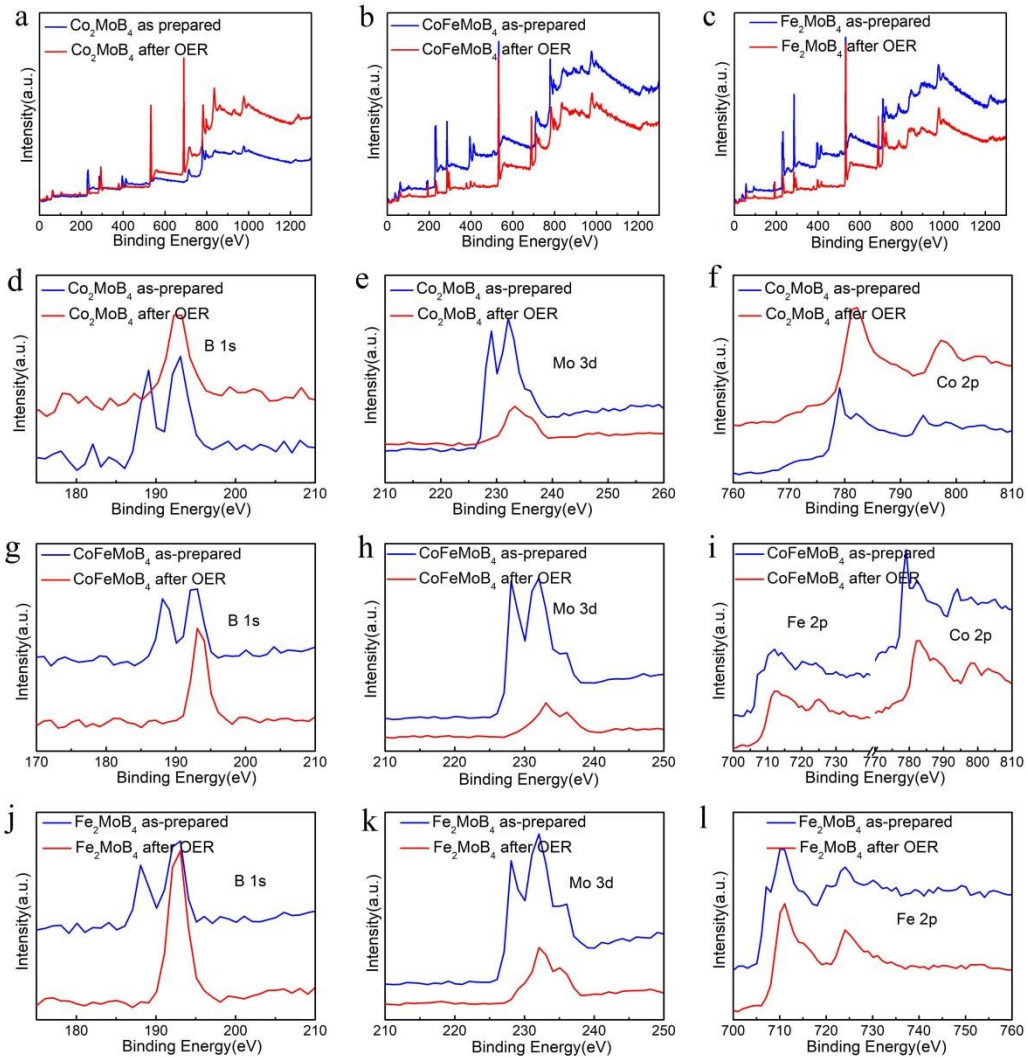

Figure S11. The survey XPS spectra of (a) Co_2MoB_4, (b) $CoFeMoB_4$, and (c) Fe_2MoB_4; (d) B 1s, (e) Mo 3d, (f) Co 2p spectra are enlarged partial areas of (a) Co_2MoB_4; (g) B 1s, (h) Mo 3d, (i) Fe 2p and Co 2p spectra are enlarged partial areas of (b) $CoFeMoB_4$; (j) B 1s, (k) Mo 3d, (l) Fe 2p spectra are enlarged partial areas of (c) Fe_2MoB_4.

Figure S12. High-resolution XPS spectra of $CoFeMoB_4$ before and after OER. (a) B 1s; (b) O 1s.

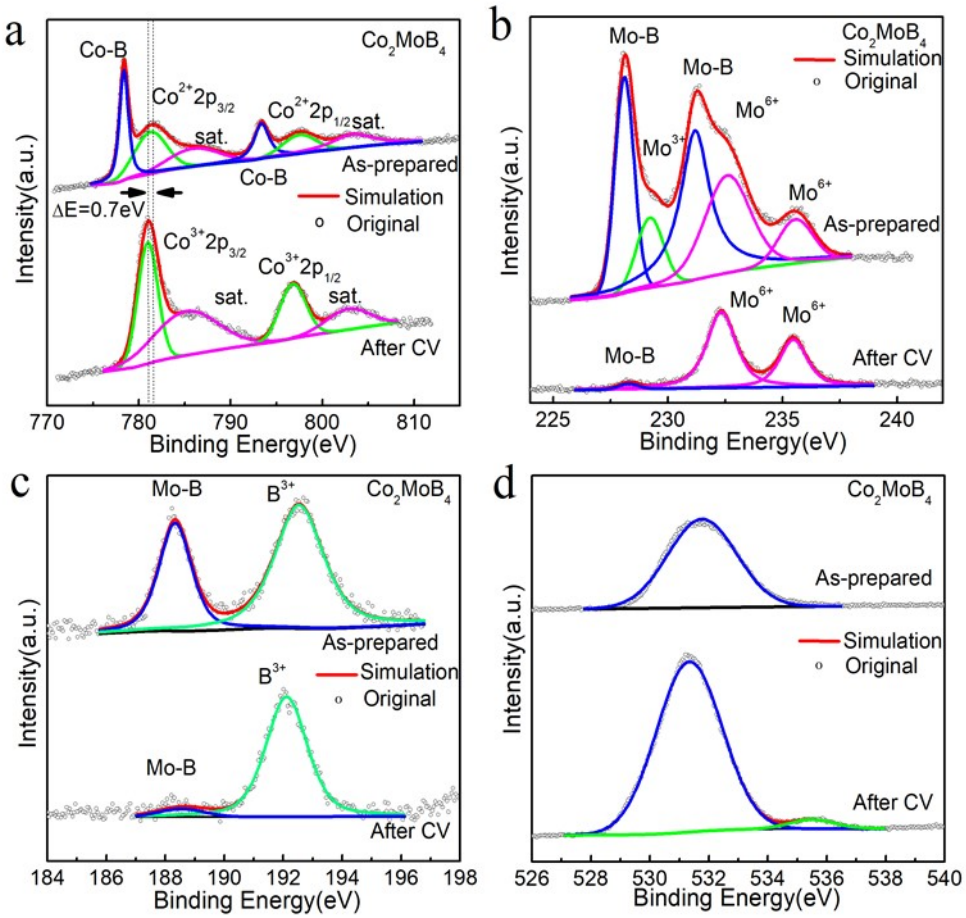

Figure S13. High-resolution XPS spectra of Co_2MoB_4 before and after OER. (a) Co 2p; (b) Mo3d; (c) B1s; and (d) O1s.

Figure S14. High resolution XPS spectra of Fe_2MoB_4 before and after OER. (a) Fe 2p; (b) Mo 3d; (c) B 1s; and (d) O1s.

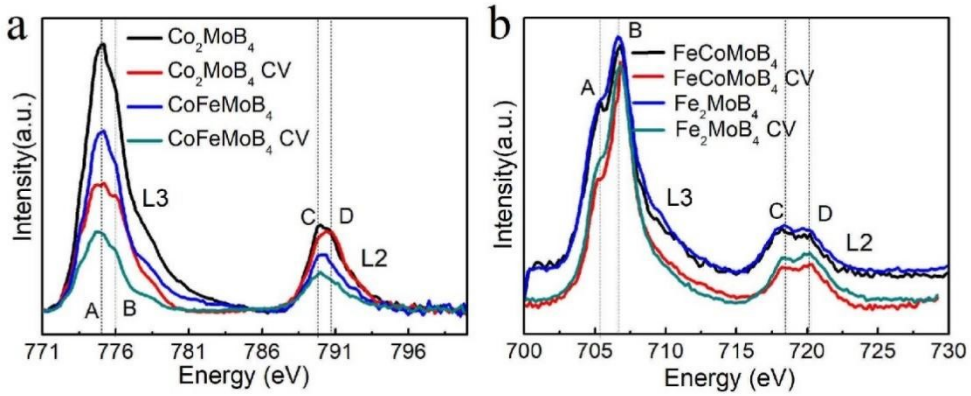

Figure S15. (a) Surface-sensitive TEY XAS scans for Co L-edge before and after OER; (b) Surface-sensitive TEY XAS scans for Fe L-edge before and after OER.

Figure S16. The extended X-ray absorption spectra of the $CoFeMoB_4$ catalyst before and after OER. Fourier transformed $k^3\chi(k)$oscillations measured at (a) Co K-edge; (b) Fe K-edge; and (c) Mo K-edge.

Figure S17. The extended X-ray absorption spectra of $CoFeMoB_4$ catalyst after OER. Fourier transformed $k^3\chi(k)$ oscillations measured at Co K-edge and fitted by different models: (a) Co_2MoB_4; (b) Co_2MoB_4 and CoOOH; and (c) Co_2MoB_4 and CoO.

Figure S18. The extended X-ray absorption spectra of the $CoFeMoB_4$ catalyst after OER. Fourier transformed $k^3\chi(k)$ oscillations measured at the Fe K-edge and fitted by different models: (a) Fe_2MoB_4; and (b) Fe_2MoB_4 and Fe_2O_3.

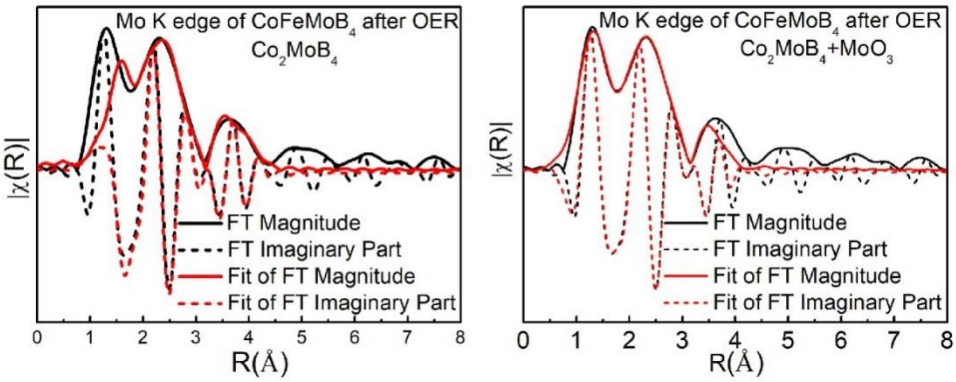

Figure S19. X-ray absorption spectra of the $CoFeMoB_4$ catalyst after OER. Fourier transformed $k^3\chi(k)$ oscillations measured at the Mo K-edge and fitted by the Co_2MoB_4 structure(left) and fitted by structure of Co_2MoB_4 and MoO_3(right). The diversity of first peak is induced by oxygen coordination.

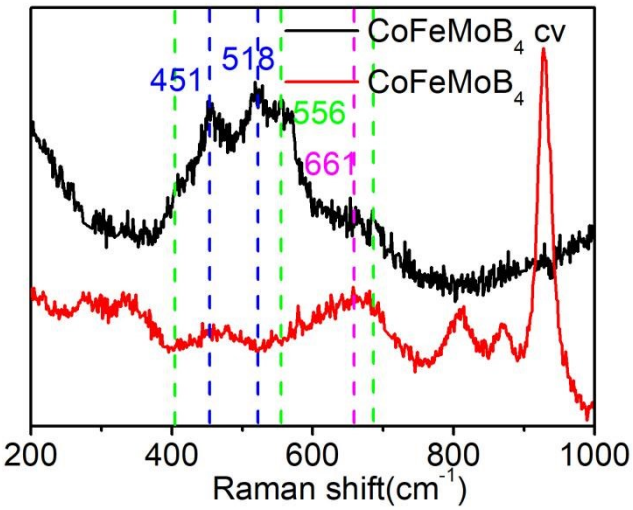

Figure S20. Raman shift of $CoFeMoB_4$ before and after OER.The bands located at around 451, 518 cm^{-1} are associated with the α-$Co(OH)_2$ structure. The band observed at 451cm^{-1} is assigned to the OCoO (A_{1g}) bending mode and the band at 520 cm^{-1} is attributed to the CoO (A_{2u}) symmetric stretching mode.[43] The weak peak near 661 cm^{-1} is the A1g mode of γ-CoOOH suggesting there is a small amount of γ-CoOOH. The peaks around 400, 556, and 690 cm^{-1} stem from α-FeOOH. [44]Thus, an evident amount of $Co(OH)_2$ and FeOOH appears on the sample after the OER reaction and there may also be a tiny amount of CoOOH.

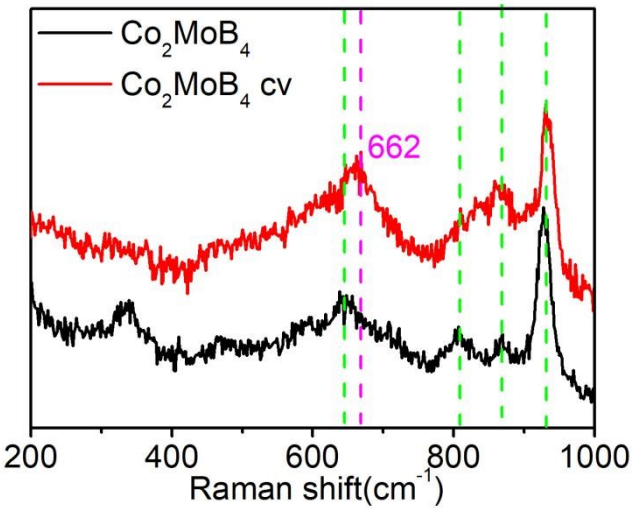

Figure S21. Raman shift of Co_2MoB_4 before and after OER. The peak near 662 cm^{-1} of Co_2MoB_4 after OER is the A_{1g} mode of γ-CoOOH suggesting it is the product of CoOOH during the electrochemical reaction[43].

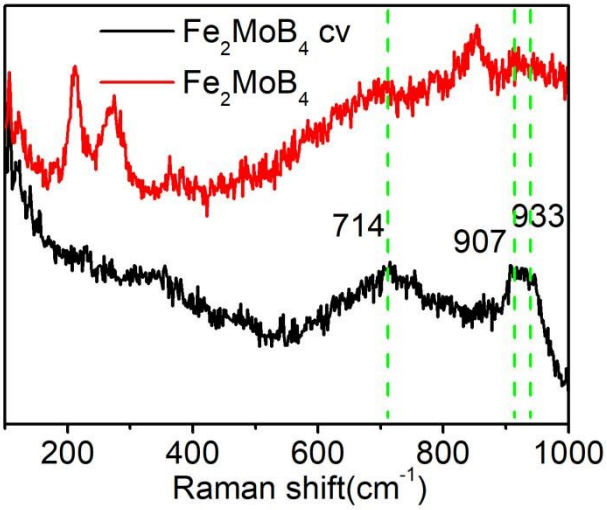

Figure S22. Raman shift of Fe_2MoB_4 before and after OER. The broad peak at around 714 cm^{-1} suggest the formation of Fe_2O_3[45], and the peak between 907 cm^{-1} to 933cm^{-1} is related to the motions of the oxygen atoms connecting two MO_6 octahedrons [46].

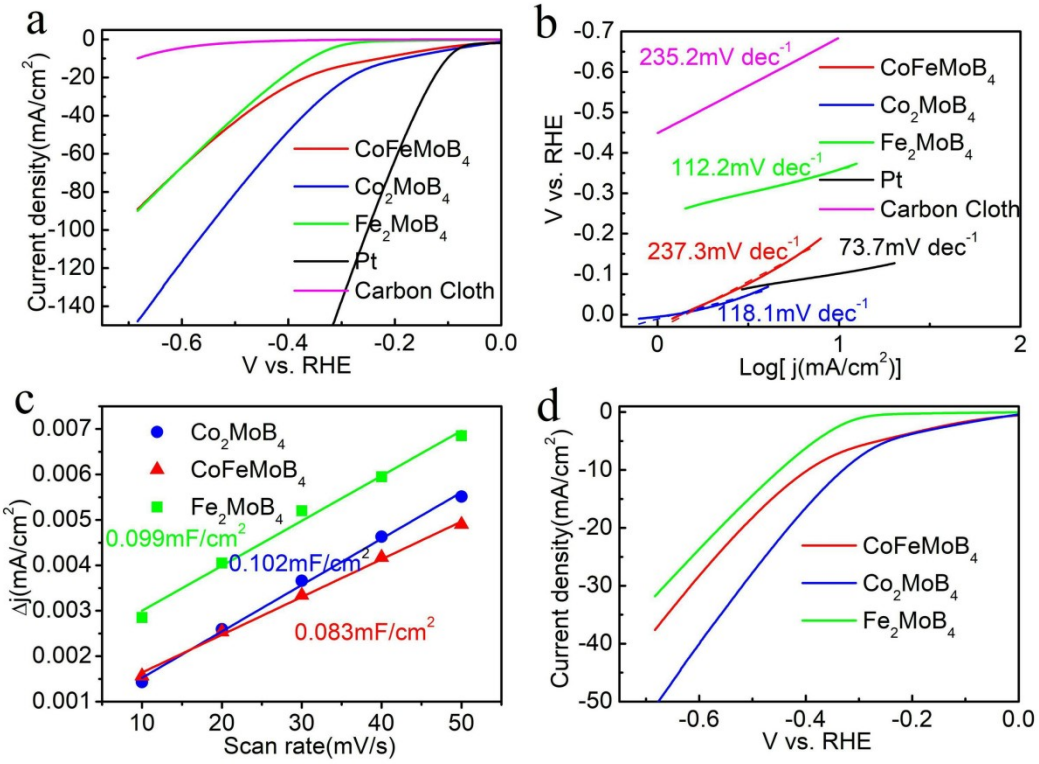

Figure S23. (a) Linear sweep voltammetry curves toward HER without iR compensation and (b) Tafel slopes of $CoFeMoB_4$, Fe_2MoB_4, Co_2MoB_4, Pt slice with area of 1cm^2 and carbon cloth. (c) ECSA of different samples calculated by cyclic voltammetry at non-Faraday region. (d) ECSA normalized LSC curves[42]

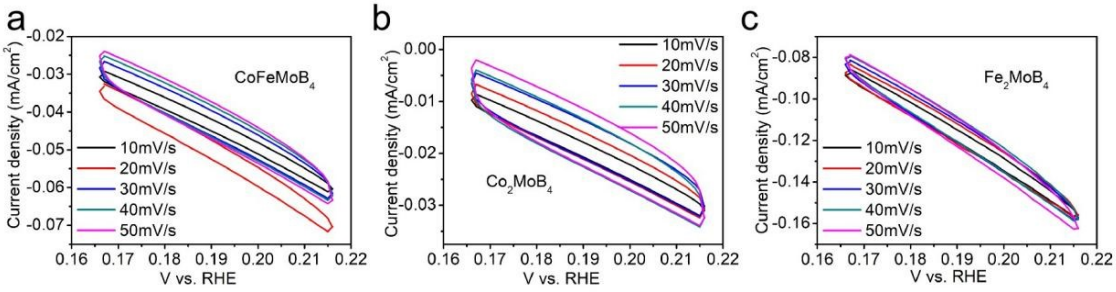

Figure S24. CV curves at different scan rates of (a) $CoFeMoB_4$, (b) Co_2MoB_4 and (c) Fe_2MoB_4 .

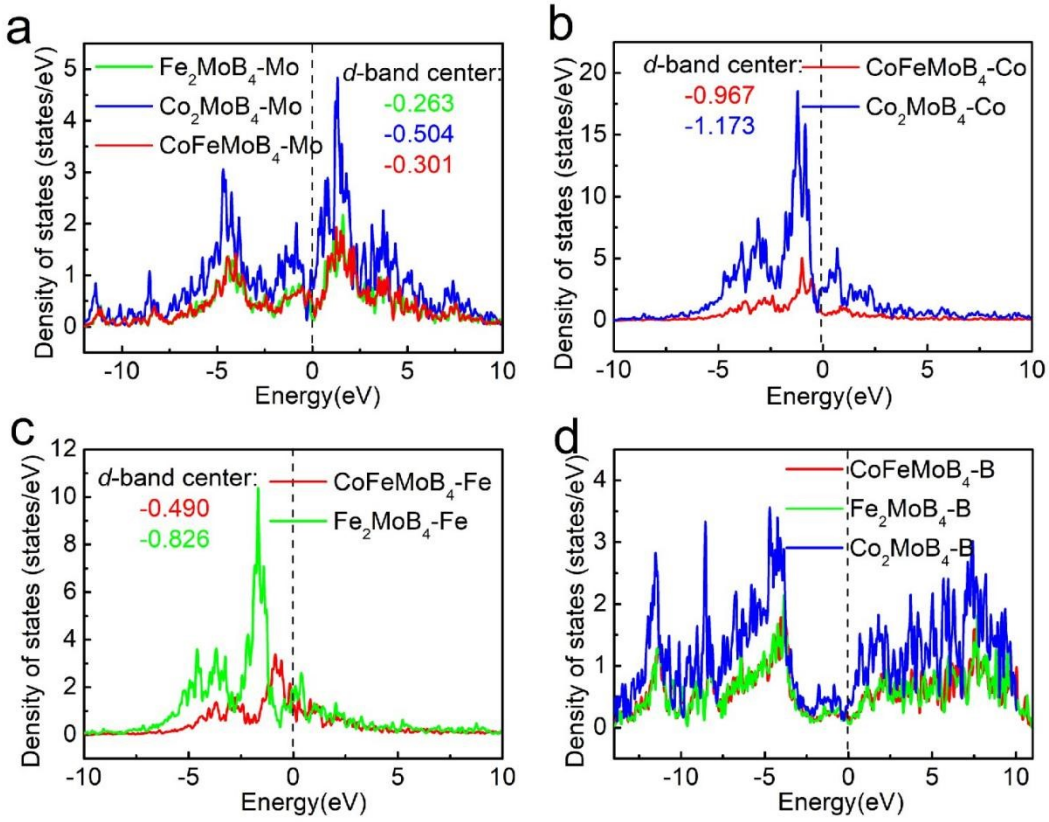

Figure S25. Spin up orbital (a) Mo-4d DOS of $CoFeMoB_4$, Co_2MoB_4 and Fe_2MoB_4; (b) Co-3d DOS of $CoFeMoB_4$ and Co_2MoB_4; (c) Fe-3d DOS of $CoFeMoB_4$ and Fe_2MoB_4; (d) B-sp DOS of $CoFeMoB_4$, Co_2MoB_4 and Fe_2MoB_4 .

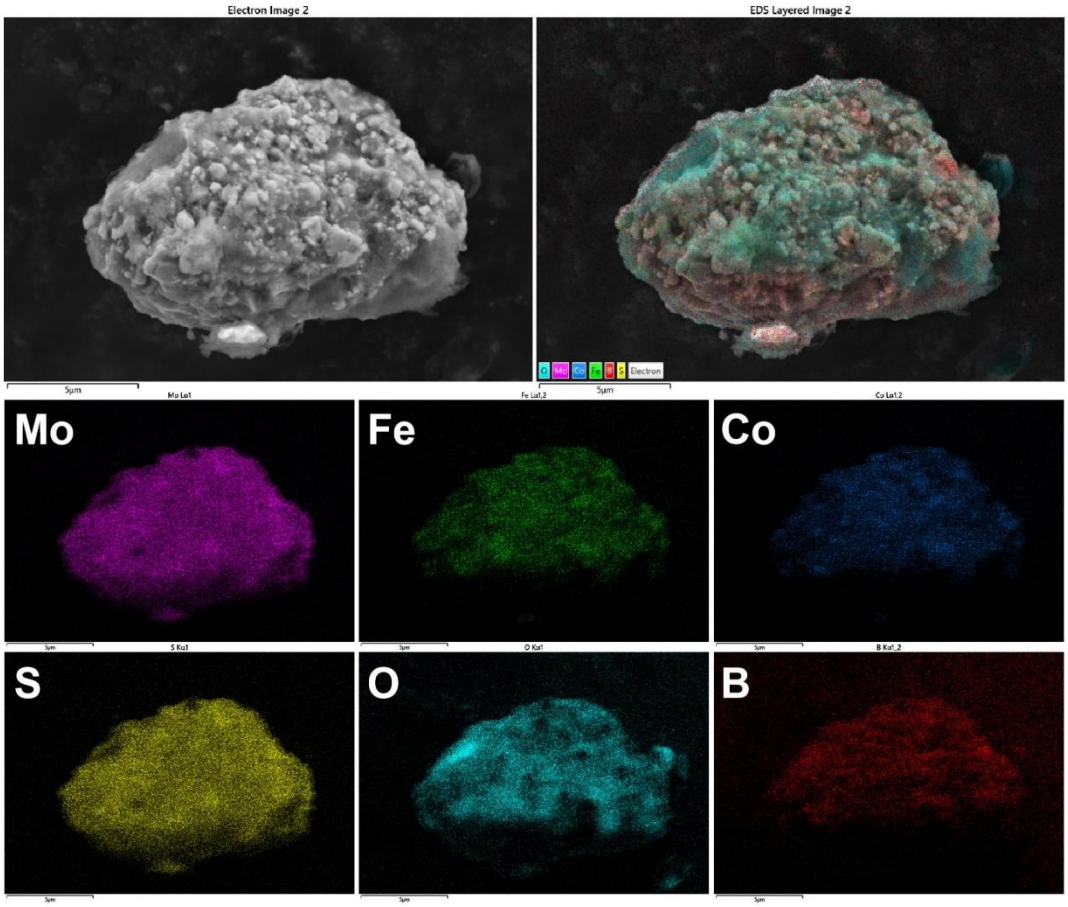

Figure S26. SEM images of $CoFeMoB_4$ after HER measured in 0.5M H_2SO_4 electrolyte.

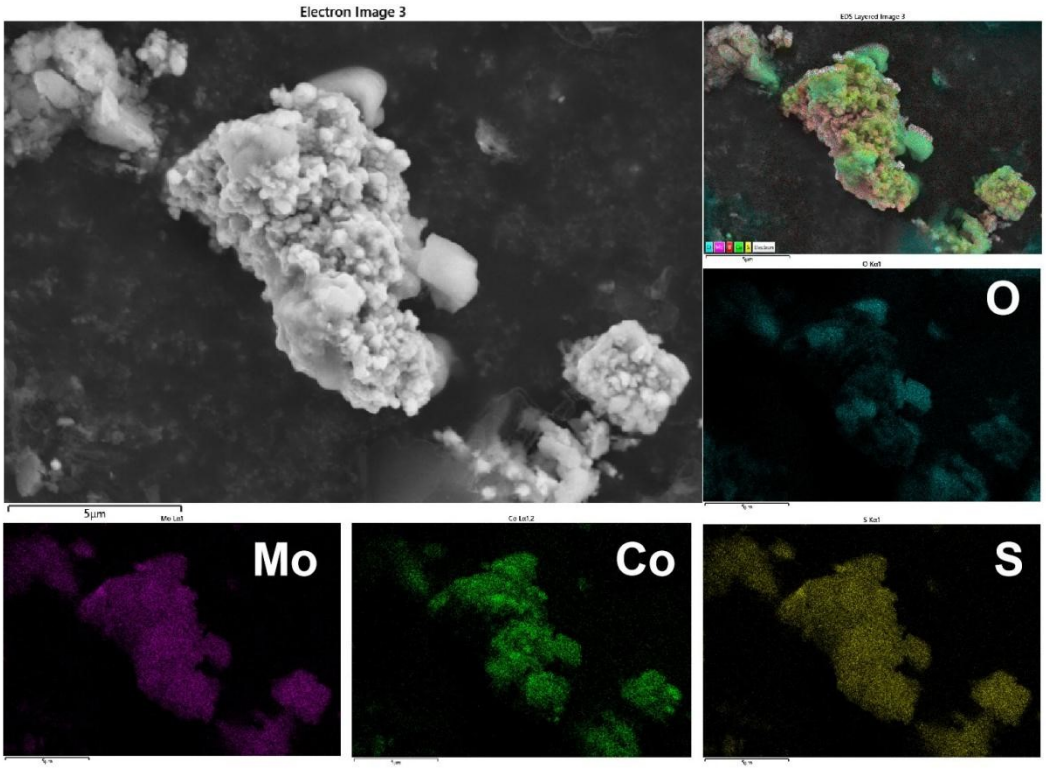

Figure S27. SEM images of Co_2MoB_4 after HER measured in 0.5M H_2SO_4 electrolyte.

Reference

[1] G. Kresse, J. Hafner, *Phys. Rev. B* **1993**, *47*, 558-561.

[2] G. Kresse, J. Furthmüller, *Comput. Mater. Sci.* **1996**, *6*, 15-50.

[3] J. P. Perdew, K. Burke, M. Ernzerhof, *Phys. Rev. Lett.* **1996**, *77*, 3865-3868.

[4] J. P. Perdew, K. Burke, Y. Wang, *Phys. Rev. B* **1996**, *54*, 16533-16539.

[5] C. Elsässer, M. Fähnle, C. T. Chan, K. M. Ho, *Phys. Rev. B* **1994**, *49*, 13975-13978.

[6] S. Wang, P. He, Z. Xie, L. Jia, M. He, X. Zhang, F. Dong, H. Liu, Y. Zhang, C. Li, *Electrochim. Acta* **2019**, *296*, 644-652.

[7] J. Sun, W. Zhang, S. Wang, Y. Ren, Q. Liu, Y. Sun, L. Tang, J. Guo, X. Zhang, *J. Alloys Compd*. **2019**, *776*, 511-518.

[8] J. M. V. Nsanzimana, L. Gong, R. Dangol, V. Reddu, V. Jose, B. Y. Xia, Q. Yan, J. M. Lee, X. Wang, *Adv. Energy Mater*. **2019**, *9*, 1901503.

[9] Y. Jiang, Y. Fang, C. Chen, P. Ni, B. Kong, Z. Song, Y. Lu, L. Niu, *ChemElectroChem* **2019**, *6*, 3684-3689.

[10] J. Li, H. Chen, Y. Liu, R. Gao, X. Zou, *J. Mater. Chem. A* **2019**, *7*, 5288-5294.

[11] J. Masa, P. Weide, D. Peeters, I. Sinev, W. Xia, Z. Sun, C. Somsen, M. Muhler, W. Schuhmann, *Adv. Energy Mater*. **2016**, *6*, 1502313.

[12] J. M. V. Nsanzimana, Y. Peng, Y. Y. Xu, L. Thia, C. Wang, B. Y. Xia, X. Wang, *Adv. Energy Mater*. **2018**, *8*, 1701475.

[13] S. Gupta, N. Patel, R. Fernandes, S. Hanchate, A. Miotello, D. C. Kothari, *Electrochim. Acta* **2017**, *232*, 64-71.

[14] J. Masa, I. Sinev, H. Mistry, E. Ventosa, M. de la Mata, J. Arbiol, M. Muhler, B. Roldan Cuenya, W. Schuhmann, *Adv. Energy Mater*. **2017**, *7*, 1700381.

[15] N. Xu, G. Cao, Z. Chen, Q. Kang, H. Dai, P. Wang, *J. Mater. Chem. A* **2017**, *5*, 12379-12384.

[16] W. J. Jiang, S. Niu, T. Tang, Q. H. Zhang, X. Z. Liu, Y. Zhang, Y. Y. Chen, J. H. Li, L. Gu, L. J. Wan, J. S. Hu, *Angew. Chem., Int. Ed.* **2017**, *56*, 6572-6577.

[17] J. Jiang, M. Wang, W. Yan, X. Liu, J. Liu, J. Yang, L. Sun, *Nano Energy* **2017**, *38*, 175-184.

[18] W. Lu, T. Liu, L. Xie, C. Tang, D. Liu, S. Hao, F. Qu, G. Du, Y. Ma, A. M. Asiri, X. Sun, *Small* **2017**, *13*, 1700805.

[19] H. Li, P. Wen, Q. Li, C. Dun, J. Xing, C. Lu, S. Adhikari, L. Jiang, D. L. Carroll, S. M. Geyer, *Adv. Energy Mater*. **2017**, *7*, 1700513.

[20] K. Elumeeva, J. Masa, D. Medina, E. Ventosa, S. Seisel, Y. U. Kayran, A. Genç, T. Bobrowski, P. Weide, J. Arbiol, M. Muhler, W. Schuhmann, *J. Mater. Chem. A* **2017**, *5*, 21122-21129.

[21] H. Chen, S. Ouyang, M. Zhao, Y. Li, J. Ye, *ACS Appl. Mater. Interfaces* **2017**, *9*, 40333-40343.

[22] Y. Li, H. Xu, H. Huang, L. Gao, Y. Zhao, T. Ma, *Electrochem. Commun*. **2018**, *86*, 140-144.

[23] M. Arivu, J. Masud, S. Umapathi, M. Nath, *Electrochem. Commun*. **2018**, *86*, 121-125.

[24] G. Liu, D. He, R. Yao, Y. Zhao, J. Li, *Nano Res*. **2018**, *11*, 1664-1675.

[25] J. M. V. Nsanzimana, V. Reddu, Y. Peng, Z. Huang, C. Wang, X. Wang, *Chemistry* **2018**, *24*, 18502-18511.

[26] Z. Chen, Q. Kang, G. Cao, N. Xu, H. Dai, P. Wang, *Int. J. Hydrogen Energy* **2018**, *43*, 6076-6087.

[27] Y. Li, B. Huang, Y. Sun, M. Luo, Y. Yang, Y. Qin, L. Wang, C. Li, F. Lv, W. Zhang, S. Guo, *Small* **2019**, *15*, e1804212.
[28] S. Chen, Y. Li, Z. Zhang, Q. Fu, X. Bao, *J. Mater. Chem. A* **2018**, *6*, 10644-10648.
[29] W. Hao, R. Wu, R. Zhang, Y. Ha, Z. Chen, L. Wang, Y. Yang, X. Ma, D. Sun, F. Fang, Y. Guo, *Adv. Energy Mater.* **2018**, *8*, 1801372.
[30] S. Klemenz, J. Schuch, S. Hawel, A.-M. Zieschang, B. Kaiser, W. Jaegermann, B. Albert, *ChemSusChem* **2018**, *11*, 3150-3156.
[31] X. Liang, R. Dong, D. Li, X. Bu, F. Li, L. Shu, R. Wei, J. C. Ho, *ChemCatChem* **2018**, *10*, 4555-4561.
[32] J. M. V. Nsanzimana, R. Dangol, V. Reddu, S. Duo, Y. Peng, K. N. Dinh, Z. Huang, Q. Yan, X. Wang, *ACS Appl. Mater. Interfaces* **2019**, *11*, 846-855.
[33] X. Chen, Z. Yu, L. Wei, Z. Zhou, S. Zhai, J. Chen, Y. Wang, Q. Huang, H. E. Karahan, X. Liao, Y. Chen, *J. Mater. Chem. A* **2019**, *7*, 764-774.
[34] W. Yuan, X. Zhao, W. Hao, J. Li, L. Wang, X. Ma, Y. Guo, *ChemElectroChem* **2019**, *6*, 764-770.
[35] M. J. Kirshenbaum, M. H. Richter, M. Dasog, *ChemCatChem* **2019**, *11*, 3877-3881.
[36] D. K. Mann, J. Xu, N. E. Mordvinova, V. Yannello, Y. Ziouani, N. Gonzalez-Ballesteros, J. P. S. Sousa, O. I. Lebedev, Y. V. Kolen'ko, M. Shatruk, *Chem. Sci.* **2019**, *10*, 2796-2804.
[37] F. Guo, Y. Wu, H. Chen, Y. Liu, L. Yang, X. Ai, X. Zou, *Energy Environ. Sci.* **2019**, *12*, 684-692.
[38] L. Wang, J. Li, X. Zhao, W. Hao, X. Ma, S. Li, Y. Guo, *Adv. Mater. Interfaces* **2019**, *6*. 1801690.
[39] T. Tan, P. Han, H. Cong, G. Cheng, W. Luo, *ACS Sustainable Chem. Eng.* **2019**, *7*, 5620-5625.
[40] H. Han, Y. R. Hong, J. Woo, S. Mhin, K. M. Kim, J. Kwon, H. Choi, Y. C. Chung, T. Song, *Adv. Energy Mater.* **2019**, *9*, 1803799.
[41] L. Cagnon, T. Devolder, R. Cortes, A. Morrone, J. E. Schmidt, C. Chappert, P. Allongue, *Phys. Rev. B* **2001**, *63*, 104419.
[42] C. C. L. McCrory, S. Jung, I. M. Ferrer, S. M. Chatman, J. C. Peters and T. F. Jaramillo, J. Am. Chem. Soc., **2015**, *137*, 4347 – 4357.
[43] L. Aguilera, P. C. M. Aguiar, Y. L. Ruiz, A. Almeida, J. A. Moreira, R. R. Passos, L. A. Pocrifka, *J. Mater. Sci: Mater. Electron* **2020**, *31*, 3084-3091.
[44] W. D. Chemelewski, H. C. Lee, J. F. Lin, A. J. Bard, C. B. Mullins, *J. Am. Chem. Soc.* **2014**, *136*, 2843-2850.
[45] C. Rémazeilles, P. Refait, *Corros. Sci.* **2007**, *49*, 844-857.
[46] G. D. Saraiva, J. A. Lima, F. F. de Sousa, J. H. da Silva, V. O. Sousa Neto, A. J. Ramiro de Castro, J. Mendes Filho, *Vib. Spectrosc.* **2018**, *94*, 89-94.